RSC Advances

PAPER

View Article Online
View Journal | View Issue

Cite this: *RSC Adv.*, 2025, **15**, 17388

Constructing binder-free 3D thermal networks with hexagonal boron nitride of varying sizes to enhance polydimethylsiloxane composites: a comparative study†

Liping Han,‡[ab] Hu Sun,‡[a] Wei Li,[a] Li Liu,[bc] Guoyou Gan,[b] Zhuo Qian*[b] and Junpeng Li*[a]

As electronic devices become more compact and power-dense, the demand for efficient thermal management materials continues to rise. To address the common issues in conventional thermally conductive composites—namely, poor filler dispersion, high interfacial thermal resistance caused by binders, and complex fabrication processes—this study proposes a novel strategy for constructing binder-free three-dimensional hexagonal boron nitride thermal networks (3D BN) within a polydimethylsiloxane (PDMS) matrix. By leveraging the decomposition behavior of ammonium bicarbonate (NH_4HCO_3), this approach enables the fabrication of composites with enhanced thermal conductivity and simplified processing. The 3D BN/PDMS composites were prepared *via* a straightforward process involving blending, cold pressing, drying, and vacuum impregnation. Characterization and testing reveal that the 3D BN thermal network and BN particle size are critical factors influencing the composites' TCs. The resulting 3D BN/PDMS composites exhibit an outstanding TC of 3.889 W m^{-1} K^{-1} when the BN particle size is 20 μm and the filler content is 40.70 vol%. This study offers a novel approach to designing and developing high-performance thermally conductive composites, with significant potential for practical applications.

Received 19th February 2025
Accepted 28th April 2025

DOI: 10.1039/d5ra01204j

rsc.li/rsc-advances

1. Introduction

As the power density of electronic devices continues to increase, the heat generated during operation also rises significantly, creating a pressing need for efficient thermal management solutions to ensure device stability and reliability.[1–3] Thermal interface materials (TIMs), positioned between heat sources and heat sinks, effectively fill microscopic gaps, reducing interfacial thermal resistance and facilitating rapid heat transfer to the heat sink.[4–6] By utilizing TIMs with excellent TC, the operating temperature of electronic devices can be significantly lowered, thereby extending their lifespan, enhancing performance, and preventing failures caused by overheating.[7–9] Due to their vital role in thermal management, TIMs are widely used in high-power-density devices such as computer processors, LED lighting systems, and power semiconductors.[10,11]

PDMS is considered an ideal base material for thermal management because of its excellent processability, chemical stability, and electrical insulation properties.[12–14] However, the intrinsic thermal conductivity of PDMS is relatively low (approximately 0.2 W m^{-1} K^{-1}), which limits its ability to meet the thermal management requirements of modern high-power electronic devices. As a result, incorporating thermally conductive fillers into PDMS has become an effective strategy to enhance its thermal conductivity.[15–18] These PDMS-based composites maintain the flexibility of the polymer while offering superior thermal management performance. In the study of thermally conductive fillers, various materials, including carbon nanotubes,[19,20] graphene,[21,22] silver,[23,24] boron nitride,[25,26] and alumina,[27,28] have been explored to enhance the thermal conductivity of composites. However, the electrical conductivity of metallic and carbon-based fillers limits their application in insulation-critical fields, making ceramic fillers the preferred choice. Among these, hexagonal boron nitride (BN) stands out as an ideal candidate for high-performance, electrically insulating thermally conductive composites. BN exhibits an in-plane thermal conductivity of ~200 W m^{-1} K^{-1} and out-of-plane thermal conductivity of ~30 W m^{-1} K^{-1}, along

[a]Sino-Platinum Metals Co., Ltd, Kunming 650106, People's Republic of China. E-mail: lijunpeng@ipm.com.cn

[b]Faculty of Material Science and Engineering, Kunming University of Science and Technology, Kunming 650093, People's Republic of China. E-mail: 20210067@kust.edu.cn

[c]School of Electrical Engineering, Chongqing University of Arts and Sciences, Chongqing 402160, People's Republic of China

† Electronic supplementary information (ESI) available. See DOI: https://doi.org/10.1039/d5ra01204j

‡ These authors contributed equally to this work.

with excellent electrical insulation, thermal stability, and low dielectric constant.[29,30] Although recent developments have demonstrated remarkable thermal conductivities using advanced filler architectures—such as vertically aligned boron nitride nanoribbons (BNNRs)[31] and BN microspheres assembled from nanosheets[32]—these approaches often involve complex alignment techniques or template-assisted synthesis, which may hinder scalability.

However, incorporating large amounts of BN into polymers often leads to suboptimal thermal and mechanical properties. This is primarily due to the strong van der Waals forces between BN layers, which cause agglomeration and hinder uniform dispersion within the polymer matrix. Such agglomeration creates discontinuities in the thermal conduction pathways, reducing the composite's overall thermal conductivity. Additionally, the inert surface of BN exhibits poor interfacial compatibility with the polymer matrix, resulting in significant interfacial thermal resistance, which impedes heat transfer from the polymer to the thermally conductive filler, further compromising the composite's thermal conductivity.

To overcome these challenges, researchers have proposed strategies for constructing three-dimensional thermal networks based on BN to enhance the thermal conductivity of composites. For example, Qin *et al.*[33] used melamine sponge (MS) as a framework, coated with boron nitride nanosheets (BNNSs), and employed polyvinyl alcohol (PVA) as a binder to successfully fabricate a 3D-networked BNNS@MS/PVA composite hydrogel. This composite achieved a thermal conductivity of 1.12 W m^{-1} K^{-1} at a BNNSs content of approximately 6 wt%, which is twice that of pure hydrogel. Similarly, Pan *et al.*[34] utilized freeze-drying technology to construct a vertically aligned network structure of cellulose/m-SiC nanowires/m-BN/resin aerogel (CA/m-SiC/m-BN/EP), with cellulose acting as the binder. This composite exhibited a vertical in-plane thermal conductivity as high as 2.21 W m^{-1} K^{-1} while maintaining significantly improved insulation performance. Our previous research explored two innovative approaches to enhancing the thermal conductivity of polymer-based composites. In one study,[29] we developed a novel composite featuring a dual thermal network structure of BN and Al_2O_3, utilizing polyimide (PI) as the binder and epoxy resin (EP) as the matrix. The results demonstrated that when the composite contained 17.67 wt% BN and 26.23 wt% Al_2O_3, it achieved a thermal conductivity of 1.077 W m^{-1} K^{-1}, marking a 496% improvement over pure EP. In another study,[30] we employed a hard-template method using PMMA microspheres as sacrificial materials and a small amount of PVA as a binder to fabricate a lightweight 3D BN@Ag/EP composite with high thermal conductivity and excellent dielectric properties. With a filler content of 26 wt%, the composite reached a thermal conductivity of 1.381 W m^{-1} K^{-1}, demonstrating the effectiveness of this approach in enhancing thermal performance. These studies demonstrate that using binders (typically polymers) to support the 3D BN thermal network in composites can enhance thermal conductivity. However, the presence of binders between the thermally conductive fillers increases interfacial thermal resistance, which impedes efficient heat transfer between the fillers. This resistance significantly diminishes the effectiveness of the 3D thermal network.[35,36] Therefore, constructing a binder-free 3D BN in composites remains a major challenge.

Inspired by numerous studies that employ sacrificial template methods, such as salt-templating[37,38] and ice-templating techniques,[35,39] to construct 3D BN, this study uses NH_4HCO_3 as a sacrificial template. Leveraging its thermal decomposition into gaseous products, we constructed a dense, binder-free 3D BN thermal network within a PDMS matrix to enhance the composite's TC. Through processes such as blending, cold pressing, and heating, a self-supporting, binder-free 3D BN was formed. Subsequently, PDMS was infiltrated into the 3D BN *via* vacuum impregnation. Following this preparation method, we successfully fabricated 3D BN/PDMS composites with excellent TC. Through comparative experiments and finite element simulations, we systematically investigated the effects of the 3D BN, BN particle size, and distribution on the TCs of the composites.

2. Experimental section

2.1 Materials

BN (2, 11, 20, 40 μm) was purchased from Shanghai Zhongye New Material Co., Ltd. NH_4HCO_3 (decomposition temperature is above 36 °C) was supplied by Shanghai Macklin Biochemical Co., Ltd. PDMS (Sylgard 184, 1.03 g cm^{-3}) was obtained from Dow Corning New Materials Co., Ltd.

2.2 Preparation of 3D BN and 3D BN/PDMS composites

As depicted in Fig. 1, BN and NH_4HCO_3 of varying sizes were mixed in equal mass ratios (1 : 1). The mixture was compressed at 10 MPa for 10 minutes using a tablet press to form 1.2 g bulk BN/NH_4HCO_3 samples with demotion of 40 × 10 × 1.5–2 mm. These samples were then placed in 30 mL polytetrafluoroethylene (PTFE) containers and dried at 75 °C for 12 hours to ensure complete decomposition of NH_4HCO_3, resulting in the formation of the 3D BN. Subsequently, 2 g PDMS (precursor : curing agent = 9 : 1 by mass) was carefully poured into the PTFE containers containing the 3D BN. The mixture was vacuum-impregnated for 5 hours to replace air voids in the 3D BN with PDMS. Finally, the samples were cured at 100 °C for 5 hours to yield the 3D BN/PDMS composites. Composites containing BN of varying particle sizes (2 μm, 11 μm, 20 μm, and 40 μm) were labeled BP-1, BP-2, BP-3, and BP-4, respectively. For comparison, randomly distributed BN/PDMS composites with the same BN content as the BP series were prepared using mechanical mixing method[40,41] and designated as rBP-1, rBP-2, rBP-3, and rBP-4.

2.3 Characterization

The microstructure of the composites was observed using a scanning electron microscope (SEM, Nova NanoSEM 450, FEI, USA) operated at an accelerating voltage of 10 kV. Elemental distribution was characterized using an energy-dispersive X-ray spectrometer (EDS) attached to the SEM. The phase structure of BN particles with different sizes was analyzed *via* X-ray

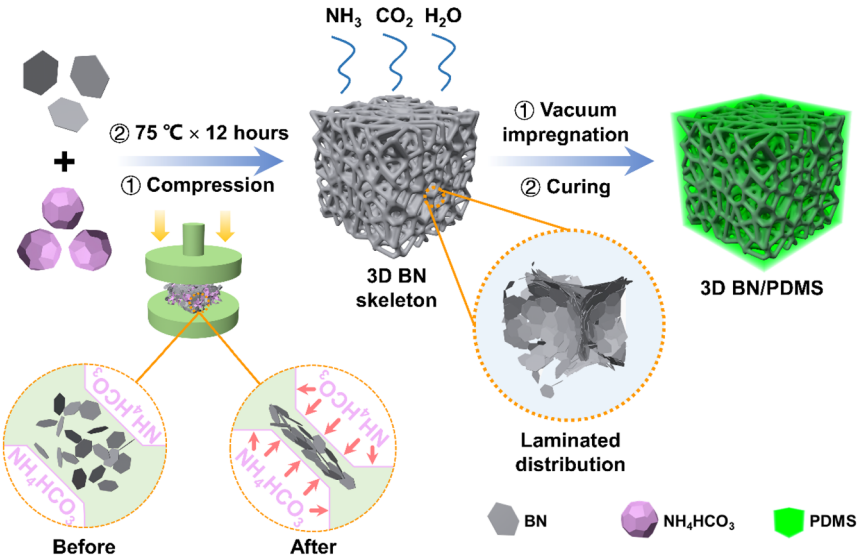

Fig. 1 Schematic diagram of the fabrication process of 3D BN/PDMS composite.

diffraction (XRD, Empyrean, PANalytical B.V., Netherlands) using Cu Kα radiation ($\lambda = 0.154$ nm), with a scanning range of 10–80° and a scanning speed of 5° min^{-1}. The thermal stability of the composites was evaluated using a thermogravimetric analyzer (TGA, Q1000, TA) under a nitrogen atmosphere to prevent oxidative degradation and ensure accurate evaluation of thermal stability, from 30 to 800 °C at a heating rate of 10 °C min^{-1}. The coefficient of thermal expansion (CTE) of the composites was measured using a thermomechanical analyzer (TMA, model TMA 402 F1 E1, Netzsch) in the temperature range of 25–150 °C, with a preload force of 0.02 N and a heating rate of 5 °C min^{-1}. The TCs (κ) of the composites were calculated using the formula:

$$\kappa = \alpha \times \rho \times C_p$$

where α is the thermal diffusivity ($mm^2\ s^{-1}$), measured at 25 °C using a laser flash analyzer (LFA 467, NETZSCH, Germany); ρ is the density of the composites (g cm^{-3}), determined *via* the Archimedes method; and C_p is the specific heat capacity (J g^{-1} K^{-1}), measured using a differential scanning calorimeter (DSC, Discovery DSC, TA Corporation, USA). The temperature evolution on the surface of the heated samples over time was recorded using an infrared thermal imaging camera (260 B, UTI). The compressive strength of the composites was determined using a universal testing machine (CMT6104, SENS) under a loading rate of 0.2 mm min^{-1} in the resin casting body compression testing mode, with samples in the form of cylinders with a diameter of 10 mm and a thickness of 1.5–2 mm.

3. Results and discussion

3.1 Filler morphology and phase analysis

Fig. 2(a)–(d) show the SEM images of BN particles with varying sizes. All samples exhibit a lamellar structure with smooth surfaces and are free from impurities. The well-preserved crystalline structure is crucial for maintaining the intrinsic TC of the raw material.[1] Fig. 2(e) presents the XRD patterns of BN with different particles sizes. All samples display characteristic BN peaks at 26.76°, 41.60°, 43.87°, 50.15°, 55.16°, and 75.93°, with no additional peaks. According to the standard PDF card for BN (JCPDS#34-0421), these peaks correspond to the (002), (100), (101), (102), (004), and (110) crystal planes, respectively. This confirms that the BN particles used in the experiments retain an intact crystalline structure, with no significant defects.

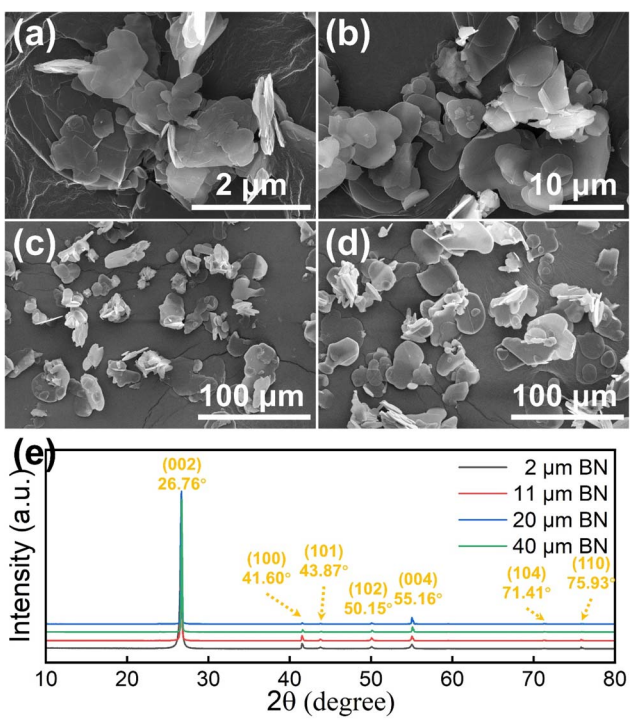

Fig. 2 SEM images of (a) 2 μm BN, (b) 11 μm BN, (c) 20 μm BN and (d) 40 μm BN. (e) XRD patterns of BN with different sizes.

3.2 Morphology analysis of composites

A continuous 3D thermal network is essential for determining the thermal conductivity of composites.[42] However, the self-supporting 3D BN obtained after the removal of NH_4HCO_3 is too fragile to be directly characterized by SEM. Fig. 3(k) shows the EDS mapping images of BP-4, where the dark, smooth regions correspond to PDMS (indicated by Si distribution), and the regions representing the 3D BN are shown by B distribution. Fig. 3(a)–(d) display low-magnification SEM images of the cross-sections of the BP series composite. The intact 3D BN structures observed in all samples suggest that the prefabricated self-supporting 3D BN can withstand the pressure exerted by PDMS during the vacuum infiltration process. PDMS effectively fills the pores of the 3D BN and maintains an interconnected state after curing, which is crucial for establishing continuous thermal conduction pathways in the composite. Furthermore, no unfilled pore regions left by NH_4HCO_3 decomposition were observed in any of the samples, indicating excellent compatibility between the constructed 3D BN and PDMS in this study.

It is well established that sheet-like BN exhibits anisotropic thermal conductivity, with in-plane TC significantly higher than through-plane TC.[43] Thus, the distribution of sheet-like BN significantly influences the TC of the composite. The rigid NH_4HCO_3 particles compress the BN into their interstitial spaces, causing sheet-like BN near the NH_4HCO_3 particles to align perpendicular to the applied pressure. However, due to the irregular crystal structure of NH_4HCO_3, the size of the interstitial spaces varies randomly during cold pressing. Both the gap size and the size of BN particles influence the final distribution of BN.

Fig. 3(e)–(h) show magnified SEM images of the cross-sections of the BP series composite, highlighting the distribution of BN particles with varying sizes. Notably, no polymer-based adhesive is present between the BN particles in any of the samples, preventing significant filler-to-filler interfacial thermal resistance typically introduced by materials with inherently low thermal conductivity.[36] As shown in Fig. 3(e), in BP-1 (with 2 μm BN), most BN particles exhibit a relatively disordered distribution, with only a small fraction forming stacked layers near the PDMS interface. This suggests that during cold pressing, NH_4HCO_3 particles induce only a limited number of 2 μm BN particles to form stacked layers, resulting in a low-quality 3D layered thermal network. However, as the BN particle size increases, Fig. 3(f)–(h) show a progressive increase in the proportion of stacked BN particles, with stacked BN layers forming the foundation of a high-quality thermal network. Nonetheless, since BN is a rigid material, larger BN particles lead to greater porosity within the 3D BN, which significantly reduces the density of the thermal network.

3.3 Thermal conductivities of composites

TC is a critical metric for evaluating the performance of thermally conductive composites. In this study, the mass ratio of BN to NH_4HCO_3 in all samples was fixed at 1 : 1 during preparation, ensuring consistent filler content across all samples. Based on the TGA curve of BP-3, the filler content in the composites was calculated to be approximately 40.70 vol% (detailed calculations are provided in Fig. S1†). Fig. 4(a) shows the TCs of the composite samples. For reference, the TC of pure PDMS was measured at 0.187 W m^{-1} K^{-1}. Overall, the TCs of the rBP series composites exceed 1 W m^{-1} K^{-1}, significantly higher than that

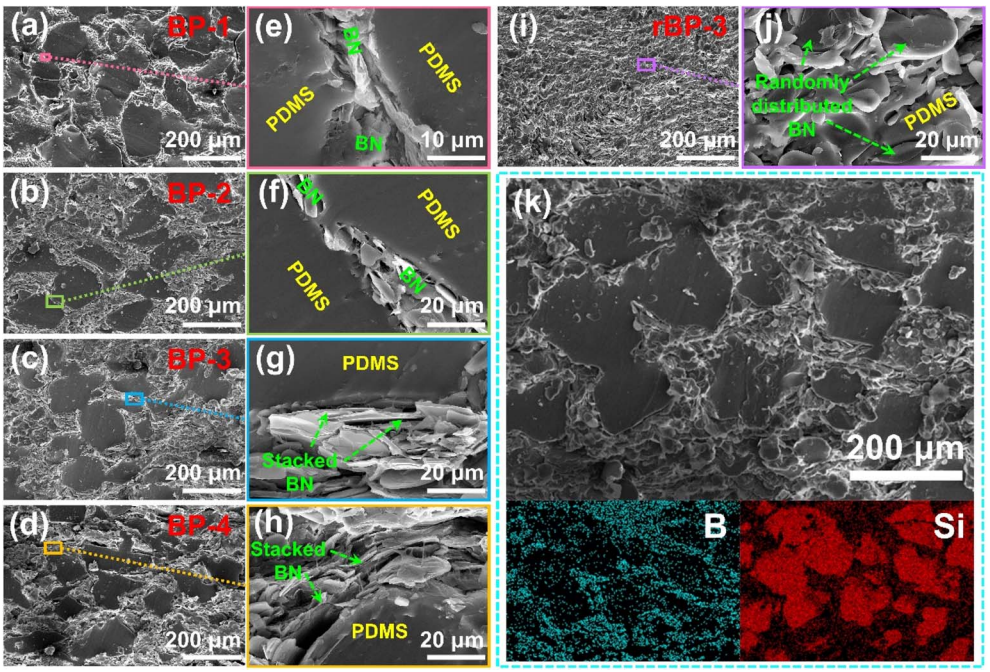

Fig. 3 SEM images and corresponding enlarged images of (a) and (e) BP-1, (b) and (f) BP-2, (c) and (g) BP-3, (d) and (h) BP-4, and (i) and (j) rBP-3. (k) EDS mapping images of BP-4.

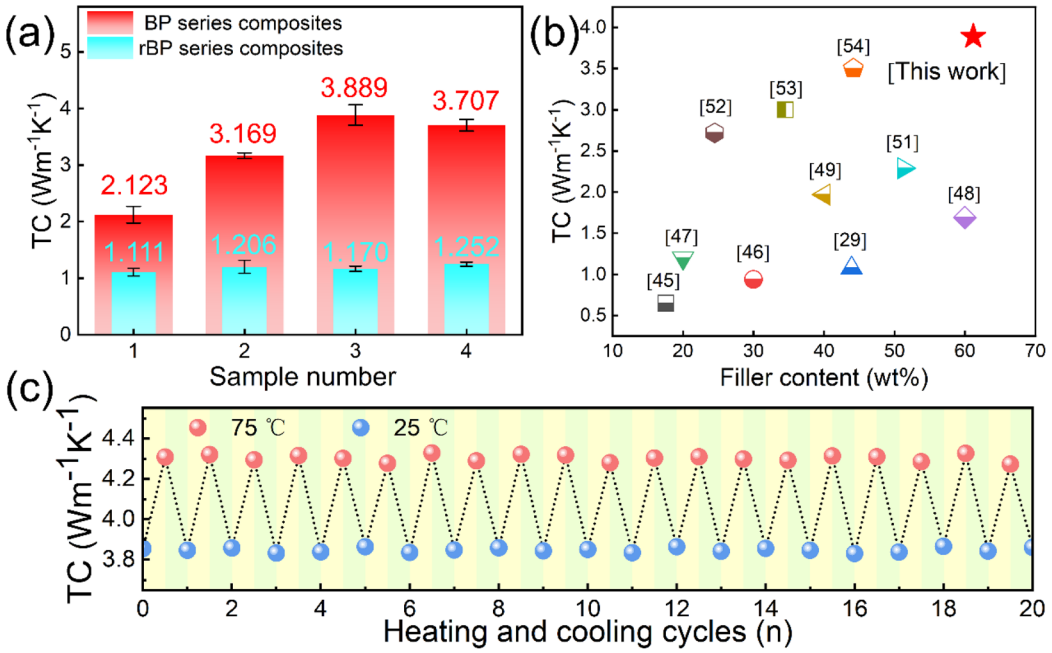

Fig. 4 (a) The TCs of composites at room temperature. (b) Comparison of the TCs of polymer matrix composites reinforced by BN reported in recent years. (c) The TCs of BP-3 composite during 10 thermal cycles.

of pure PDMS. This indicates that the incorporation of BN effectively enhances the TCs of the composites. However, BN particle size does not appear to have a substantial impact on the TCs of the rBP series composites. For the BP series composites, the TCs range from 2 to 4 W m^{-1} K^{-1}, which is notably higher than the 1–1.3 W m^{-1} K^{-1} observed for the rBP series composites. This highlights the advantage of using NH_4HCO_3 to pre-construct the 3D BN. Additionally, as the BN particle size increases, the TCs of the BP series composites initially rise and then decrease. This trend is attributed to the distribution of BN particles and the density of the thermal network. The BN distribution can be inferred from the SEM characterization, while the density of the thermal network correlates positively with the composite density,[44] as shown in Table S1.† As the BN particle size increases, the density of the thermal network decreases. For BP-1, the thermal network density is the highest in the BP series. However, the proportion of BN particles forming high-quality stacked layers is relatively small due to the limited alignment of the 2 μm BN particles during cold pressing. Moreover, with the same filler content, BP-1 contains a greater number of BN particles, which increases filler–filler interfacial thermal resistance. These factors result in a TC of only 2.123 W m^{-1} K^{-1} for BP-1. As the BN particle size increases to 20 μm (BP-3), the thermal network density decreases slightly, but a higher proportion of BN particles align to form stacked layers, constructing a higher-quality thermal network. Additionally, the reduced number of BN particles in BP-3 compared to BP-1 minimizes filler–filler interfaces and reduces interfacial thermal resistance, leading to a TC of 3.889 W m^{-1} K^{-1}. In BP-4 (with 40 μm BN), although a high proportion of stacked BN layers is observed, the network density decreases significantly due to increased porosity in the 3D BN. This results in fewer contact points between rigid BN particles, hindering heat transport and leading to a slightly lower TC of 3.707 W m^{-1} K^{-1} compared to BP-3. These results indicate that, in the strategy of using NH_4HCO_3 as a hard-template method to fabricate 3D BN/PDMS composites, the BN particle size creates a competitive relationship between the quality and density of the 3D thermal network. This competition ultimately determines the composite's TC.

Fig. 4(b) compares the TCs of polymer matrix composites reinforced by BN, showcasing various structures reported in recent years.[29,45–54] The results highlight the superiority of our NH_4HCO_3 hard-template strategy for preparing 3D BN/PDMS composites. TIMs frequently undergo temperature fluctuations during electronic device operation. The stability of the TCs is crucial, as TIMs must maintain consistent performance across temperature variations to ensure reliable heat dissipation.[55]

To assess the stability and reliability of our composites under practical conditions, Fig. 4(c) presents the TC of BP-3 during thermal cycling between 25 °C and 75 °C. The results show that BP-3 maintains stable TCs of approximately 3.8 W m^{-1} K^{-1} at 25 °C and 4.3 W m^{-1} K^{-1} at 75 °C over 10 thermal cycles, with no significant fluctuations. This demonstrates the excellent thermal stability of BP-3 under thermal cycling, making it suitable for applications in environments with temperature fluctuations.

To further explore the influence of different distribution states of the thermally conductive filler BN on heat transfer performance, we conducted transient finite element simulations of local regions within PDMS, BP-3, and rBP-3 composites using COMSOL Multiphysics 6.1. The simulations were based on the generalized heat transfer equation within the solid heat

transfer module, and were informed by previous studies.[56] A qualitative analysis was performed to assess the thermal conduction behavior. In the rBP-3 model, BN is uniformly distributed within the PDMS matrix. Each mesh element in this model was treated as a homogeneous mixture of BN and PDMS, requiring only the overall thermal conductivity parameters of the composite. In the BP-3 model, PDMS regions were modeled as spheres based on the size of NH_4HCO_3. Details of the model dimensions and thermal conductivity parameters are provided in the supplementary materials (Table S2†). The initial ambient temperature for all models was set to 293.15 K, with the bottom surface defined as a constant-temperature heat source at 373.15 K, the sides thermally insulated, and the top surface subject to natural convection. To capture transient heat transfer, the simulation time step was set to 0.1 ms, with a total simulation duration of 2 ms. Fig. 5 illustrates the volumetric temperature distributions of the models. In the PDMS and rBP-3 models, heat propagates slowly and uniformly upward from the bottom surface, with the rBP-3 model exhibiting a faster heat transfer rate compared to the PDMS model. In contrast, the BP-3 model shows significantly enhanced overall thermal conductivity. Further analysis of the heat flux directions within the composites (Fig. S2†) reveals that in the PDMS and rBP-3 models, heat flux propagates vertically without distinct thermal pathways due to the homogeneous nature of the materials. However, in the BP-3 model, heat flux preferentially follows the 3D BN, emphasizing the advantage of pre-constructing this network within PDMS. This difference in heat transfer rates is also reflected in the temperature distribution of the top surfaces over time (Fig. S3†). At 2 ms, the average temperature of the top surface in the BP-3 model reaches 326.63 K, significantly higher than the 293.15 K in the PDMS model and 293.17 K in the rBP-3 model.

3.4 Thermal management and thermal expansion performance of composites

The primary function of thermally conductive composites is to efficiently transfer heat from a heat source to a heat sink. To visually demonstrate the thermal management capabilities of different structural composites, samples of PDMS, rBP-3, and BP-3 were placed on a heating stage (Fig. S4†), and the surface temperature changes were recorded using a handheld infrared thermal imaging device. Temperature changes were monitored from the moment the heating stage was activated until 180 seconds, to evaluate the thermal management performance. The surface temperature of the material directly reflects its thermal management effectiveness, with a higher surface temperature at a given time indicating better heat transfer efficiency and thermal management performance.

Fig. 6(a) presents both physical images and infrared thermal images of the composites. At time 0 s, all three composites had the same initial temperature. However, after 10 seconds of heating, noticeable differences in surface temperatures emerged. The surface temperature of BP-3 reached 30.4 °C, significantly higher than that of rBP-3 and PDMS. From 10 s to 180 s, the surface temperatures of the composites consistently followed the order: BP-3 > rBP-3 > PDMS. This pattern indicates that, under identical heterogeneous interface conditions, BP-3 exhibits superior thermal management performance compared to both rBP-3 and PDMS.

During installation and operation, TIMs are typically subjected to compressive forces. This compression helps eliminate air gaps between the heat source and the heat sink, thereby minimizing interfacial thermal resistance. Consequently, adequate compressive strength is essential to ensure that the composite material maintains structural integrity under load and that the internal thermal network remains intact.[57–59] To investigate the effect of a thermally optimal 3D BN on the

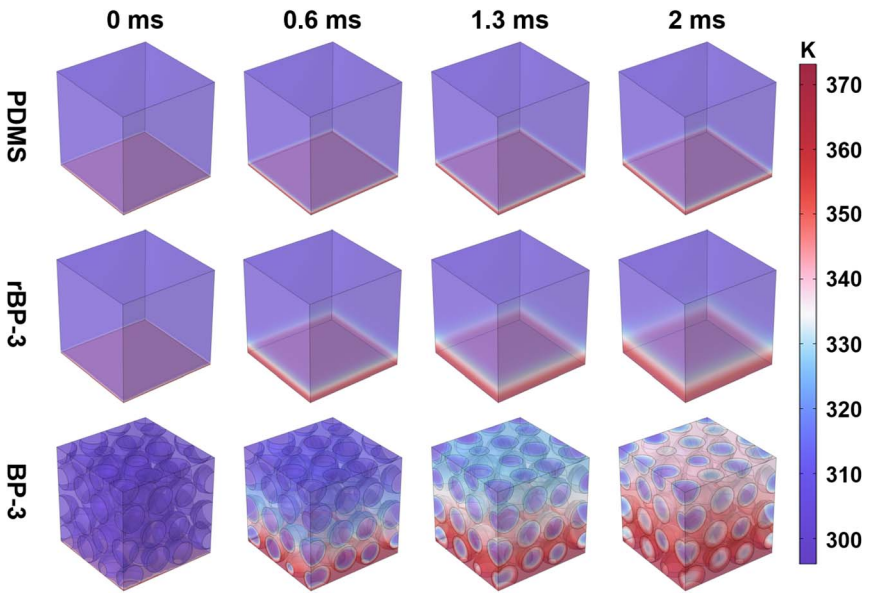

Fig. 5 Finite element simulation of heat transfer in different models.

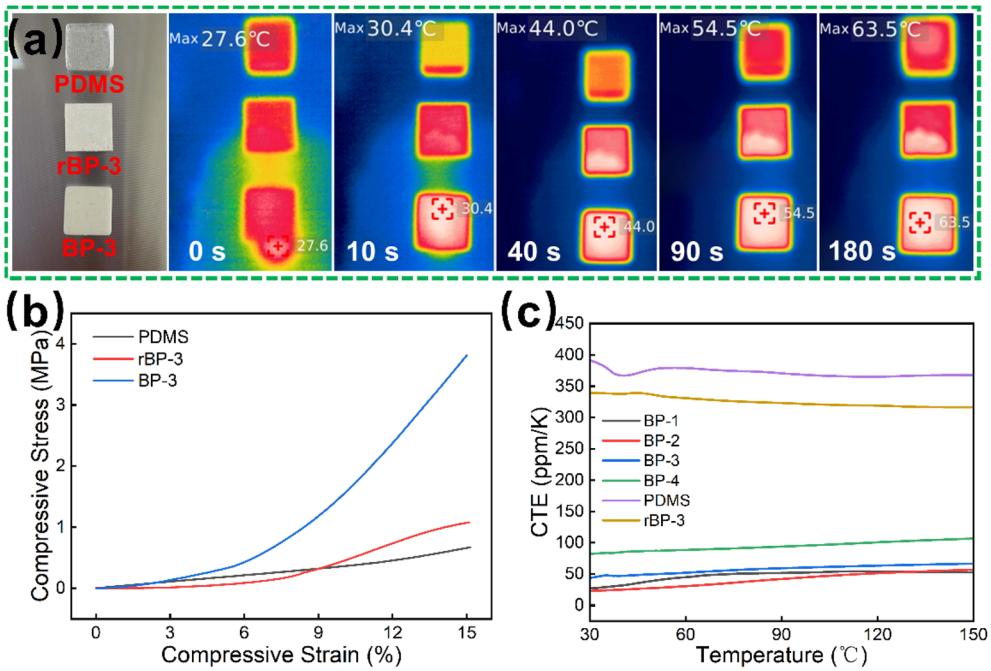

Fig. 6 (a) Optical images and infrared thermal images of the composites. (b) Compressive stress–strain curves of PDMS, rBP-3, and BP-3. (c) The CTE curves of the composites.

compressive stress of PDMS-based composites, we selected three representative samples: PDMS, rBP-3, and BP-3. As shown in Fig. 6(b), the compressive stress–strain behavior of the samples was evaluated up to 15% strain. The compressive stress of PDMS and rBP-3 was measured to be 0.67 MPa and 1.08 MPa, respectively. The increase observed in rBP-3 is likely due to the enhanced rigidity imparted by BN and the reduced PDMS content. Notably, the BP-3 sample exhibited a substantially higher compressive stress of 3.81 MPa, indicating that the presence of a 3D BN structure significantly restricts the deformation of the PDMS matrix. In contrast, randomly dispersed BN in rBP-3 exerted a lesser constraint on matrix deformation. These findings further suggest that the incorporation of a 3D BN helps preserve a stable thermal conduction pathway within the composite under mechanical stress.

The CTE is critical for the structural stability and durability of thermally conductive composites.[60] In electronic and aerospace applications, these composites are often used alongside other materials. Variations in the CTE between materials can lead to interfacial stress concentrations, causing interface damage or even material cracking, which compromises thermal pathways and reduces heat transfer efficiency. Therefore, a low CTE is beneficial, as it helps materials maintain dimensional stability under temperature fluctuations, ensuring long-term reliable thermal performance and mechanical integrity.[61] In this study, PDMS, BP series composites, and rBP-3 composites were selected to investigate the impact of BN particle sizes and the 3D BN on the CTE of PDMS-based composites. Fig. 6(c) shows the temperature-dependent CTE curves for all samples. Pure PDMS exhibits the highest CTE, reaching 367.88 ppm K^{-1} at 150 °C. Due to the ultra-low CTE of BN (in-plane CTE: −2.7 ppm K^{-1}; out-of-plane CTE: 38 ppm K^{-1}),[62] the CTE of rBP-3 at 150 °C is 316.32 ppm K^{-1}, significantly lower than that of pure PDMS. The CTE of BP-3 is even lower than that of rBP-3, which can be attributed to the thermal stability provided by the 3D BN. This network effectively limits the expansion of PDMS, helping the composite maintain dimensional stability during temperature fluctuations. Moreover, the 3D BN provides structural support, dispersing stress during temperature changes and reducing the volume change of the composite material.[63] Further comparison of the CTEs of the BP series composites reveals that CTE increases with BN particle size. This is likely due to the reduced density of the thermal network as BN particle size increases, leading to a higher proportion of air in the composite. Since the thermal expansion coefficient of air is as high as 3400 ppm K^{-1}, the CTE of the BP series composites rises with increasing BN particle size.

4. Conclusion

In this study, we successfully developed a binder-free 3D BN within a PDMS matrix using a simple sacrificial templating method based on NH_4HCO_3 decomposition. By varying the particle size of micro-scale BN flakes, we systematically explored how filler size and distribution affect the thermal conductivity of the composites. Our results revealed a trade-off between the quality and density of the thermal network, with 20 μm BN flakes forming the most effective heat conduction pathways and achieving a maximum thermal conductivity of 3.889 W m^{-1} K^{-1} at a filler content of 40.7 vol%. Finite element simulations qualitatively confirmed the role of BN distribution in guiding heat flow, while thermal cycling tests demonstrated excellent

thermal stability. The composites also exhibited reduced thermal expansion and retained reasonable compressive strength, indicating their potential for use in thermal interface materials.

Data availability

The data supporting the findings of this study are available within the article and its ESI.† Additional data may be provided upon reasonable request to the corresponding author.

Author contributions

Liping Han: methodology, data curation, validation, writing – original draft, review & editing. Hu Sun: resources, data curation, visualization, writing – review & editing. Wei Li: software, formal analysis. Li Liu: investigation, resources. Guoyou Gan: conceptualization, project administration. Zhuo Qian: resources, methodology, supervision, project administration. Junpeng Li: conceptualization, supervision, project administration, resources, editing, funding acquisition, writing – review & editing.

Conflicts of interest

The authors declare that they have no known competing financial interests or personal relationships that could have appeared to influence the work reported in this paper.

Acknowledgements

This work was supported by the Major Science and Technology Project of Yunnan Province (Grant No. 202402AB080005 and 202102AB080008), the Science and Technology Projects of Yunnan Precious Metals Laboratory (Grant No. YPML-2023050206, YPML-2022050207 and YPML-20240502102).

References

1 J. W. Zha, F. Wang and B. Q. Wan, *Prog. Mater. Sci.*, 2025, **148**, 101362.
2 L. L. An, Y. L. Yu, Q. R. Cai, S. Mateti, L. H. Li and Y. I. Chen, *Prog. Mater. Sci.*, 2023, **138**, 101154.
3 Q. G. Chen, K. L. Yang, Y. Feng, L. Liang, M. H. Chi, Z. H. Zhang and X. S. Chen, *Composites, Part A*, 2024, **178**, 107998.
4 Y. S. Duan, H. T. Yu, F. Zhang, M. M. Qin and W. Feng, *Nano Res.*, 2024, **17**, 9796–9814.
5 W. Dai, Y. D. Wang, M. H. Li, L. Chen, Q. W. Yan, J. H. Yu, N. Jiang and C. T. Lin, *Adv. Mater.*, 2024, **36**, 2311335.
6 Y. Lin, P. L. Li, W. J. Liu, J. Chen, X. Y. Liu, P. K. Jiang and X. Y. Huang, *ACS Nano*, 2024, **18**, 3851–3870.
7 D. An, X. Y. Duan, S. S. Cheng, Z. Y. Zhang, B. Yang, Q. S. Lian, J. X. Li, Z. J. Sun, Y. Q. Liu and C. P. Wong, *Composites, Part A*, 2020, **135**, 105928.
8 C. Q. Liu, J. W. Yang, Y. F. Li, J. Fu, W. Yu and H. Q. Xie, *Surf. Interfaces*, 2024, **47**, 104204.
9 J. K. Liu, H. Y. Feng, J. Y. Dai, K. R. Yang, G. M. Chen, S. P. Wang, D. D. Jin and X. Q. Liu, *Chem. Eng. J.*, 2023, **469**, 143963.
10 C. L. Liu, X. Y. Duan, W. Zhang, Q. Q. Huo, X. W. Sui, Y. Q. Liu and C. B. Liang, *Ceram. Int.*, 2024, **50**, 19829–19837.
11 X. Zhang and Z. S. Deng, *Sci. China: Technol. Sci.*, 2023, **66**, 1530–1550.
12 S. Anand, M. C. Vu, D. Mani, J. B. Kim, T. H. Jeong, M. A. Islam and S. R. Kim, *Chem. Eng. J.*, 2023, **462**, 142017.
13 M. Potenza, I. Petracci and S. Corasaniti, *Int. J. Therm. Sci.*, 2023, **188**, 108253.
14 Y. F. Zhang, L. Zhang, B. Q. Zhou, M. Ahmad, Q. Y. Zhang and B. L. Zhang, *Carbon*, 2023, **209**, 117997.
15 Y. An, R. Y. Cheng, Q. Y. Du, C. L. Li, C. H. Liu, H. Xu, F. Gao, D. M. Wu and J. Y. Sun, *Compos. Sci. Technol.*, 2023, **241**, 110119.
16 P. Wei, L. Feng, Q. Chen, Z. J. Dong, Q. Song, R. Tian, R. X. Zhang, L. Y. Guo, D. F. Xu, M. D. Hou and H. J. Song, *Chem. Eng. J.*, 2024, **488**, 150915.
17 W. Yang, Z. W. Wang, X. P. Zhu, Y. L. Zhang, Y. L. Luo and X. J. Wang, *Polymer*, 2024, **306**, 127210.
18 X. L. Zheng, K. Wu, Y. J. Zhan, H. Yang, G. M. Yuan, J. X. Wan and J. Shi, *ACS Appl. Nano Mater.*, 2024, **7**, 11803–11815.
19 A. Bashir, M. Maqbool, R. C. Lv, A. Usman, W. Aftab, H. Y. Niu, L. Kang and S. L. Bai, *Composites, Part A*, 2023, **167**, 107428.
20 J. J. Meng, J. A. Song, X. Zhang, J. Q. Wang and S. J. Li, *Compos. Commun.*, 2023, **42**, 101693.
21 S. J. Cheng, X. X. Guo, P. Tan, M. Y. Lin, J. F. Cai, Y. H. Zhou, D. F. Zhao, W. W. Cai, Y. F. Zhang and X. A. Zhang, *Composites, Part B*, 2023, **264**, 110916.
22 Y. Y. Zong, D. Y. Gui and K. M. Niu, *Mater. Today Commun.*, 2024, **38**, 108067.
23 X. D. Wu, H. J. Yu, L. Wang, X. D. Gong, D. N. Chen, Y. C. Hong and Y. H. Zhang, *Compos. Sci. Technol.*, 2023, **243**, 110268.
24 Z. Y. Zheng, H. Xu, J. L. Wen, J. F. Chen, Z. Mao, P. L. Zhu, R. Sun, W. J. Wu and J. B. Peng, *Diamond Relat. Mater.*, 2024, **141**, 110659.
25 T. Q. Huang, T. Wang, J. Jin, M. Chen and L. M. Wu, *Chem. Eng. J.*, 2023, **469**, 143874.
26 S. K. Li, B. Liu, X. Jia, M. Xu, R. Y. Zong, X. F. Li, G. H. Liu and X. L. Huai, *Ind. Eng. Chem. Res.*, 2023, **62**, 3183–3193.
27 Z. J. Lu, W. Wu, D. Drummer, Y. Wang, C. Liu, S. Li and X. T. Zhao, *Polym. Compos.*, 2023, **44**, 3221–3231.
28 W. X. Ma, L. Zhao, Q. You, L. Cui, W. L. Li, T. J. Gui and Z. B. Zhao, *Polym. Compos.*, 2024, **45**, 16541–16555, DOI: **10.1002/pc.28910**.
29 L. P. Han, L. Liu, T. Chen, Z. Qian, J. P. Li, C. Zuo and G. Y. Gan, *Polymer*, 2024, **308**, 127382.
30 L. Liu, D. Y. Bai, Y. Li, X. L. Yu, J. P. Li and G. Y. Gan, *ACS Appl. Polym. Mater.*, 2023, **5**, 8043–8052.
31 P. Wei, L. Feng, Q. Chen, Z. Dong, Q. Song, R. Tian, R. Zhang, L. Guo, D. Xu, M. Hou and H. Song, *Chem. Eng. J.*, 2024, **488**, 150915.
32 H. J. Mun, H.-B. Cho and Y.-H. Choa, *ACS Appl. Polym. Mater.*, 2024, **6**, 5058–5069.

33 M. M. Qin, Y. J. Huo, G. Y. Han, J. W. Yue, X. Y. Zhou, Y. Y. Feng and W. Feng, *J. Mater. Sci. Technol.*, 2022, **127**, 183–191.
34 D. Pan, G. Yang, H. M. Abo-Dief, J. W. Dong, F. M. Su, C. T. Liu, Y. F. Li, B. B. Xu, V. Murugadoss, N. Naik, S. M. El-Bahy, Z. M. El-Bahy, M. A. Huang and Z. H. Guo, *Nano-Micro Lett.*, 2022, **14**, 118.
35 B. Y. Hu, W. Zhang, H. Guo, S. Xu, Y. Li, M. Li and B. A. Li, *Composites, Part A*, 2022, **156**, 106891.
36 X. W. Xu, R. C. Hu, M. Y. Chen, J. F. Dong, B. Xiao, Q. Wang and H. Wang, *Chem. Eng. J.*, 2020, **397**, 125447.
37 J. Y. Jiang, H. R. Sun, J. N. ShangGuan, F. Y. Fu, X. D. Liu and S. J. Zhao, *ACS Appl. Mater. Interfaces*, 2022, **14**, 43815–43824.
38 D. Pan, Q. M. Li, W. Zhang, J. W. Dong, F. M. Su, V. Murugadoss, Y. Z. Liu, C. T. Liu, N. Naik and Z. H. Guo, *Composites, Part B*, 2021, **209**, 108609.
39 L. Y. Zhang, H. Liu, Z. H. Wang, W. B. Sui, Y. N. Gong, J. S. Cui, Y. H. Ao and L. Shang, *J. Alloys Compd.*, 2024, **985**, 173935.
40 Q. Liu, J. Tu, X. Wang, W. Yu, W. Zheng and Z. Zhao, *Carbon*, 2012, **50**, 339–341.
41 H. Kang, Y. Tang, L. Yao, F. Yang, Q. Fang and D. Hui, *Composites, Part B*, 2017, **112**, 1–7.
42 Y. X. Cui, F. Xu, D. Bao, Y. Y. Gao, J. W. Peng, D. Lin, H. L. Geng, X. S. Shen, Y. J. Zhu and H. Y. Wang, *J. Mater. Sci. Technol.*, 2023, **147**, 165–175.
43 Y. F. He, F. X. Kuang, Z. X. Che, F. Y. Sun, K. Zheng, J. N. Zhang, X. Y. Cao and Y. M. Ma, *Composites, Part A*, 2022, **157**, 106933.
44 J. F. Tan and Y. Zhang, *Molecules*, 2024, **29**, 3572.
45 X. X. Li, Q. C. Xu, Z. M. Lei and Z. X. Chen, *Ceram. Int.*, 2023, **49**, 22623–22629.
46 J. Liu, Z. Z. Zhang, M. J. Qu, J. Zhao and Z. C. Wang, *Polym. Compos.*, 2024, **45**, 9731–9740.
47 Y. Q. Yang, R. Z. Bi, W. Ren, Y. Y. Sun, H. H. Zhao and H. J. Duan, *Compos. Sci. Technol.*, 2023, **243**, 110259.
48 X. Bai, Y. H. Meng, F. Y. Zhou, C. Ge, D. D. Sun, D. H. Yang, X. F. Jiang, P. C. Dai and X. B. Wang, *J. Mater. Chem. C*, 2024, **12**, 15965–15974.
49 X. D. Wu, H. J. Yu, L. Wang, X. G. Meng, Z. K. Huang, X. W. Liu, X. D. Gong and J. Y. Liu, *Polym. Compos.*, 2023, **44**, 2966–2976.
50 N. B. D. Do, K. Imenes, K. E. Aasmundtveit, H. V. Nguyen and E. Andreassen, *Polymers*, 2023, **15**, 1552.
51 S. Sun, S. Zhang and M. Pan, *Compos. Sci. Technol.*, 2024, **253**, 110664.
52 X. Du, W. Yang, J. Zhu, L. Fu, D. Li and L. Zhou, *Compos. Sci. Technol.*, 2022, **222**, 109370.
53 Y. Hong, I. Azcune, A. Rekondo, T. Jiang, S. Zhou, T. Lowe and E. Saiz, *Adv. Funct. Mater.*, 2023, **34**, 2311193.
54 L. Alexis, J. Lee, G. A. Alvarez, S. Awale, D. S. Jesus, M. Lizcano and Z. Tian, *ACS Appl. Mater. Interfaces*, 2024, **16**, 29042–29048.
55 W. K. Xing, Y. Xu, C. Y. Song and T. Deng, *Nanomaterials*, 2022, **12**, 3365.
56 X. Xu, R. Hu, M. Chen, J. Dong, B. Xiao, Q. Wang and H. Wang, *Chem. Eng. J.*, 2020, **397**, 125447.
57 R. Bahru, M. F. M. A. Zamri, A. H. Shamsuddin, N. Shaari and M. A. Mohamed, *Int. J. Energy Res.*, 2021, **45**, 3548–3568.
58 W. Dai, T. Ma, Q. Yan, J. Gao, X. Tan, L. Lv, H. Hou, Q. Wei, J. Yu, J. Wu, Y. Yao, S. Du, R. Sun, N. Jiang, Y. Wang, J. Kong, C. Wong, S. Maruyama and C.-T. Lin, *ACS Nano*, 2019, **13**, 11561–11571.
59 F. Jiang, S. Zhou, T. Xu, N. Song and P. Ding, *Compos. Sci. Technol.*, 2021, **208**, 108779.
60 X. H. Ou, X. M. Lu, S. S. Chen and Q. H. Lu, *Eur. Polym. J.*, 2020, **122**, 109368.
61 X. H. Ou, S. S. Chen, X. M. Lu and Q. H. Lu, *Compos. Commun.*, 2021, **23**, 100549.
62 Z. Y. Lin, Y. Liu, S. Raghavan, K. S. Moon, S. K. Sitaraman and C. P. Wong, *ACS Appl. Mater. Interfaces*, 2013, **5**, 7633–7640.
63 J. He, H. Wang, Y. Gong, X. Y. Tian, Z. L. Zhang and J. Y. He, *Composites, Part B*, 2022, **233**, 109662.